Itinerant chiral ferromagnetism in a trapped Rashba spin-orbit-coupled Fermi gas

Shang-Shun Zhang,[1,2] Wu-Ming Liu,[1] and Han Pu[2,3]

[1]*Beijing National Laboratory for Condensed Matter Physics, Institute of Physics, Chinese Academy of Sciences, Beijing 100190, China*
[2]*Department of Physics and Astronomy, and Rice Center for Quantum Materials, Rice University, Houston, Texas 77005, USA*
[3]*Center for Cold Atom Physics, Chinese Academy of Sciences, Wuhan 430071, China*

We consider a repulsive two-component Fermi gas confined in a two-dimensional isotropic harmonic potential and subject to a large Rashba spin-orbit coupling. The single-particle dispersion can be tailored by the spin-orbit-coupling term, which provides an opportunity to study itinerant ferromagnetism in this system. We show that the interplay among spin-orbit coupling, correlation effect, and mean-field repulsion leads to a competition between ferromagnetic and nonmagnetic phases. The weakly correlated nonmagnetic and the ferromagnetic phases can be well described by the mean-field Hartree-Fock theory, while the transition between the ferromagnetic and a strongly correlated nonmagnetic phase is driven by beyond-mean-field quantum correlation effect. Furthermore, the ferromagnetic phase of this system possesses a chiral current density induced by the Rashba spin-orbit coupling, whose experimental signature is investigated.

I. INTRODUCTION

The synthetic non-Abelian gauge field recently realized in ultracold atomic systems [1–5] has provided a platform to study physics related to spin-orbit (SO) coupling, such as quantum spin Hall effects and topological insulators and superfluids, both of which have attracted tremendous attention in the condensed-matter community over the past few years [6,7]. SO coupled cold atoms thus serve as an ideal quantum simulator that simulates condensed-matter systems in which SO coupling plays essential roles [8,9]. On the other hand, SO coupling in cold atoms may also give rise to completely different physics due to unique features of atomic systems. One particular example along this line concerns the "dynamic" SO coupling arising from either the atom-atom interaction [10] or the coupling between the atom and a cavity photon field [11]. In the current work, we consider a Rashba SO coupled repulsive two-component Fermi gas confined by a two-dimensional (2D) isotropic harmonic potential. The trapping potential is necessary for any cold atom experiment as it provides atomic confinement. However, in the current situation, it plays an additional role: Together with the Rashba SO coupling, it produces a Landau level-like single-particle spectrum whose band flatness can be controlled by the SO coupling strength [12–14], which as we will show is crucial for the existence of magnetic phases in our system.

For a single spin-1/2 particle trapped in a 2D isotropic harmonic potential subject to Rashba SO coupling, the physics is well understood. The ground state of such a system is a half vortex [12]. An interesting feature of the system is that, under the limit of large SO coupling strength (more specifically, when the SO coupling energy scale is much larger than the harmonic level spacing), the single-particle spectrum exhibits a Landau level-like structure. In the case of an ensemble of zero temperature spin-1/2 bosons, as previous works have shown [13,14], intriguing spin textures and strongly correlated phases may emerge, which can be attributed to the near flat single-particle band structure. Our current work tries to answer the question: What happens when we have an ensemble of repulsive spin-1/2 fermions? More specifically, does this system exhibit ferromagnetism?

Based on Stoner's argument, a fermionic system in continuum may become ferromagnetic when the repulsive interaction strength exceeds a critical value [15]. In the context of a spin-1/2 Fermi gas, ferromagnetism means that the two spin species tend to phase separate to form spin domains as such a configuration obviously reduces interaction energy. Attempt to realize ferromagnetic state in repulsive Fermi gas was made by the MIT group in 2009 [16]. Although some indirect evidences were present, spin domain formation was not observed. Later it was clarified that their system suffers from strong atom loss as the atoms tend to form tightly bound dimers, and ferromagnetism was therefore not expected [17]. From perhaps a more fundamental point of view, even if a repulsive Fermi gas is stable, it is not completely clear whether a ferromagnetic state will result. This is because the Stoner's criterion is based on a mean-field argument, in which ferromagnetism arises once the mean-field repulsion overcomes the kinetic energy. It has been conjectured that, under strong repulsive interaction, the Fermi gas may form a strongly correlated nonmagnetic state [18,19] whose total energy may be lower than that of the ferromagnetic state. Here the quantum correlation effects, neglected in the mean-field argument, play a more dominant role.

In this paper, we will elucidate the relationship between ferromagnetism and interaction effects. We address this problem by an exact diagonalization (ED) method combined with a mean-field Hartree-Fock calculation. We may roughly divide the interaction effects into two parts: (1) it leads to a mean-field repulsion between the two spin species; (2) it builds up quantum correlations in the system. We will show that the former favors ferromagnetism, whereas the latter has an opposite effect. The competition between these two parts gives rise to the phase diagram shown in Fig. 1, where a ferromagnetic phase occupies a finite region in the parameter space spanned by the interaction strength and the SO coupling strength.

The structure of this paper is organized as follows: In Sec. II, we introduce our model Hamiltonian and describe the mechanism for tuning the band structure via SO coupling. In Sec. III, we describe our ED results for the ground-state
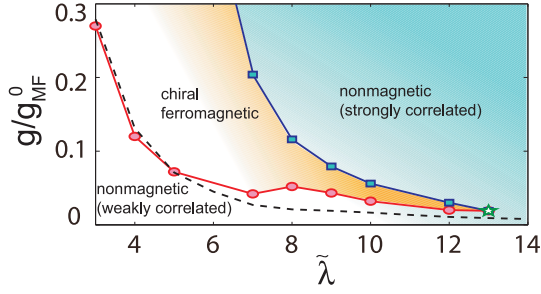
FIG. 1. Phase diagram in the g-$\tilde{\lambda}$ plane. Here we consider six repulsively interacting spin-1/2 fermions confined in a 2D harmoinc trap, subject to Rashba SO coupling. g is the interaction strength, and is normalized to $g_{MF}^0 = 2\pi\hbar^2/M$ which is the mean-field critical interaction strength for a 2D Fermi gas without SO coupling. $\tilde{\lambda}$ is the dimensionless SO coupling strength. We can see that the phase diagram contains three phases: the weakly correlated nonmagnetic phase, chiral magnetic phase, and strongly correlated nonmagnetic phase. The dashed line represents the mean-field results which contain only two regimes: a nonmagnetic phase below the dashed line and a ferromagnetic phase above the dashed line.

properties and entanglement and correlation properties. Then, in Sec. IV, we present our HF results and made comparisons with the ED calculations. The role of correlated interaction is elaborated. In what follows, we extend our previous result to systems with larger fermion number in Sec. V and explain the multiband effects. Finally, we propose an experimental method on how to detect the chiral density current in Sec. VI. A summary is given in Sec. VII.

II. MODEL

We consider a spin-1/2 Fermi gas, with atomic mass M, and chemical potential μ, confined in the x-y plane by an isotropic harmonic trap $V(r) = \frac{1}{2}M\omega r^2$ ($r = \sqrt{x^2 + y^2}$), subject to a Rashba SO coupling $\mathcal{V}_{soc} = \lambda(p_y\sigma_x - p_x\sigma_y)$, where $\sigma_{x,y}$ are Pauli matrices. The model Hamiltonian is given by $\mathcal{H} = \mathcal{H}_0 + \mathcal{H}_{int}$ where

$$\mathcal{H}_0 = \int d^2\vec{r}\,\Psi^\dagger\left[\frac{-\hbar^2\nabla^2}{2M} - \mu + \mathcal{V}_{soc} + V(r)\right]\Psi, \quad (1)$$

with $\Psi = (\Psi_\uparrow, \Psi_\downarrow)^T$ being the atomic field operator, is the single-particle Hamiltonian, and

$$\mathcal{H}_{int} = g\int d^2\vec{r}\,\Psi_\uparrow^\dagger(\vec{r})\Psi_\downarrow^\dagger(\vec{r})\Psi_\downarrow(\vec{r})\Psi_\uparrow(\vec{r}), \quad (2)$$

with $g > 0$ describes repulsive s-wave contact interaction. In what follows, we will adopt the trap units $\hbar = M = \omega = 1$, in which the units for length and energy are given by $a_{ho} = \sqrt{\hbar/(M\omega)}$ and $\hbar\omega$, respectively. Under this unit system, the interaction strength g has to be units of $\hbar\omega a_{ho}^2 = \hbar^2/M$. We also define a dimensionless SO coupling strength $\tilde{\lambda} = M\lambda a_{ho}/\hbar^2$. In the limit $\tilde{\lambda} \gg 1$, the single-particle spectrum exhibits Landau level-like structure and the curvature of each Landau band is proportional to $1/\tilde{\lambda}^2$, which provides a way to control the band flatness. Flat band structure will have two effects on an interacting many-body system: On the one hand, it may reduce the critical interaction strength for the ferromagnetic transition

according to the Stoner's criterion. On the other hand, it makes quantum correlation more pronounced. Which of these two effects become more dominant determines whether or not the system is ferromagnetic.

III. ED RESULTS

The Landau-level structure of the single-particle spectrum allows us to use the ED method to study a few-body system, where we restrict our calculation to the lowest Landau level (LLL). The single-particle Hamiltonian $\mathcal{H}_0$ conserves the total angular momentum J_z, which is the sum of the orbital and the spin angular momentum. Single-particle states in the LLL can be labeled by a single quantum number $|m\rangle$, whose total angular momentum is $J_z = m + 1/2$, and whose energy (apart from a constant) is approximately $m(m + 1)/(2\tilde{\lambda}^2)$ [12–14]. A set of such states form a Fock space basis, upon which the total Hamiltonian can be expanded [14]. For details, see Appendix A.

We present our ED results for a system of $N = 6$ fermions. Under the total Hamiltonian $\mathcal{H}$, J_z of the whole system remains as a good quantum number. Figure 2(a) displays J_z of the ground state as a function of the interaction strength g for a fixed SO coupling strength $\tilde{\lambda} = 7$. As one can see, $J_z = 0$ for small g, becomes finite for intermediate g, and vanishes again at large g. The single-particle occupation number $n_m = \langle a_m^\dagger a_m\rangle$, with a_m the annihilation operator associated with state $|m\rangle$, for the three representative cases are plotted in Figs. 2(b1)–2(b3) as a function of m. For a weakly interacting system, as shown in Fig. 2(b1), interaction induces a few particle-hole excitations near the "Fermi surface." However, the ground state still preserves the time-reversal symmetry, i.e., $n_m = n_{-m-1}$. The density profiles for the two spin species are identical. One can also calculate the local spin vector $\vec{s}(\vec{r}) = \langle\Psi^\dagger(\vec{r})\vec{\sigma}\Psi(\vec{r})\rangle$ and show that it vanishes everywhere. Hence the state is a nonmagnetic state.
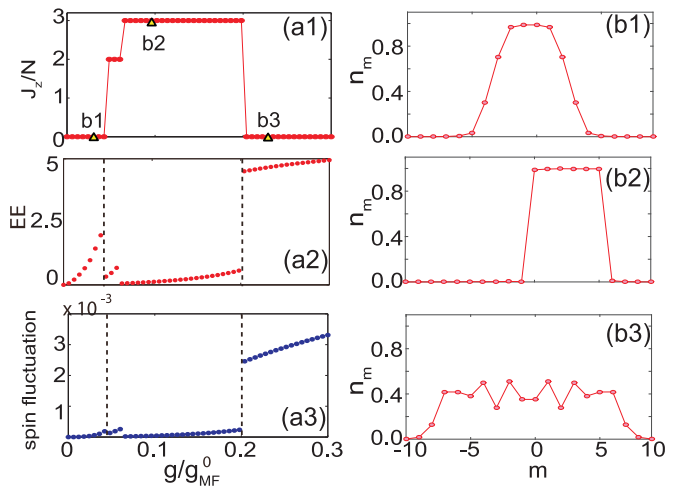

FIG. 2. Left column: (a1)–(a3) show the ground state angular momentum per particle J_z/N, entanglement entropy (EE) and ground state spin fluctuations $(\Delta S_z)^2$ as a function of interaction strength for $\tilde{\lambda} = 7, N = 6$. The non-zero J_z/N indicates a magnetic ground state. Right column: (b1)–(b3) show three representative single-particle occupation number n_m of state $|m\rangle$ for interaction strengthes marked by the yellow triangles in (a1).
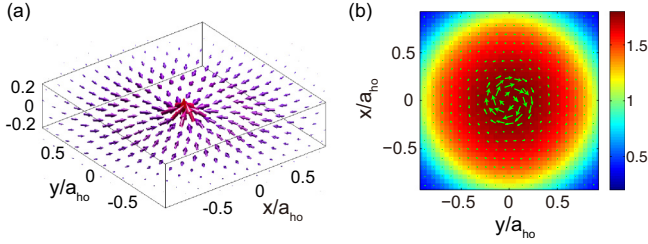
FIG. 3. (a) Spin texture of the ferromagnetic state and (b) total number density (color map) and the chiral current density (arrows) of the ferromagnetic state.

At intermediate interaction strength, as shown in Fig. 2(b2), the ground state breaks time-reversal symmetry with $n_m \neq n_{-m-1}$, the two spin species possess nonoverlapping density profiles, and nonvanishing local spin vector $\vec{s}(\vec{r})$ emerges; see Fig. 3(a). This indicates that the state is a ferromagnetic state. Furthermore, we calculated the current density of this state. With Rashba SO coupling, the current density is given by

$$\vec{j}(\vec{r}) = \sum_m \vec{j}_{\text{orbit}}^m n_m + \tilde{\lambda} \hat{z} \times \vec{s}, \tag{3}$$

where $\vec{j}_{\text{orbit}}^m = i[(\boldsymbol{\nabla}\phi_m^\dagger)\phi_m - \phi_m^\dagger\boldsymbol{\nabla}\phi_m]/2$ comes from the orbital motion where ϕ_m represents the wave function of the single-particle state $|m\rangle$. Due to the the time-reversal symmetry of the Hamiltonian, we have $\vec{j}_{\text{orbit}}^m = -\vec{j}_{\text{orbit}}^{-m-1}$. In the nonmagnetic state, $n_m = n_{-m-1}$ and $\vec{s} = 0$, both terms on the right-hand side of Eq. (3) vanish. However, for the ferromagnetic state, they are both finite, leading to a chiral current as shown in Fig. 3(b). As a result, we call the magnetic state chiral ferromagnetic. Let us comment on our result in the light of the Bloch-Bohm theorem which states that the ground state of a many-body system cannot possess finite total momentum or total angular momentum [20,21]. In the ferromagnetic phase we obtained here, the local current $\vec{j}(\vec{r}) \neq 0$, but due to rotational symmetry, we have $\vec{j}(\vec{r}) = -\vec{j}(-\vec{r})$, hence the total current $\int d\vec{r}\,\vec{j}(\vec{r}) = 0$. However, the state does possess a circulating current and hence finite angular momentum. Therefore, this state apparently violates the Bloch-Bohm theorem. To understand this point, we note that the proof of the Bloch-Bohm theorem concerning the angular momentum requires the system to be macroscopic, whereas we are concerned with a finite-size trapped system [22]. More essentially, the proof of the Bloch-Bohm theorem assumes that the system does not possess spin-orbit coupling. As a result, the Bloch-Bohm theorem does not apply to our system. Intuitively, this can be understood in the following: In a system with spin-orbit coupling, the increase in the kinetic energy due to finite (angular) momentum can be compensated by the decrease of the effective Zeeman energy associated with the interaction between the spin and the effective magnetic field. This is clearly manifested in the chiral ferromagnetic state studied here: The presence of the circulating current is always accompanied by a nontrivial spin texture.

At large interaction strength, as shown in Fig. 2(b3), the time-reversal symmetry is restored, and once again we have $\vec{s}(\vec{r}) = 0$ and $\vec{j}(\vec{r}) = 0$ as in the weakly interacting regime.

The fluctuations of n_m indicates that this nonmagnetic state is strongly correlated. To quantify the quantum correlation and fluctuation, we calculated the entanglement entropy (EE) of the system (see Appendix B), and the total spin fluctuation $(\Delta S_z)^2 = \langle \hat{S}_z^2 \rangle - \langle \hat{S}_z \rangle^2$, and plot them as functions of g in Figs. 2(a2) and 2(a3), respectively. Both EE and $(\Delta S_z)^2$ for the large interaction regime are significantly higher than those in the other two regimes.

With the above results and similar calculations for other SO coupling strengths, we can present the phase diagram as shown in Fig. 1. For $\tilde{\lambda} \lesssim 13$, there exists a window of ferromagnetic phase at intermediate values of g. As g increases from zero to a lower critical value (represented by the red solid line with filled circles), the weakly correlated nonmagnetic state becomes ferromagnetic. Note that this lower critical value is much smaller than $g_{\text{MF}}^0 = 2\pi\hbar^2/M$, the mean-field ferromagnetic critical interaction strength of a 2D Fermi gas without SO coupling [23,24]. This can be understood from the Stoner's argument and the flat band single-particle spectrum. In Ref. [25], it was shown that the critical interaction strength for ferromagnetic transition in a repulsive Fermi gas can also be reduced by adding a weak optical lattice, as the lattice potential helps to quench the kinetic energy. The essential physics here is similar to our situation. However, as g further increases to an upper critical value (represented by the blue solid line with empty squares), the ferromagnetic state gives way to a strongly correlated nonmagnetic state. As $\tilde{\lambda}$ increases, i.e., the single-particle band becomes flatter, this window of ferromagnetic phase shrinks quickly, and eventually vanishes for $\tilde{\lambda} \gtrsim 13$. At such large SO coupling strength, the single-particle band becomes so flat that a very small interaction strength gives rise to strong correlations that disfavor the ferromagnetic state.

If it is the correlation effects that destroy the ferromagnetic state, then one should not expect this to occur in a mean-field theory, which neglects quantum correlation. To examine this, we now turn to a mean-field Hartree-Fock calculation.

IV. HARTREE-FOCK RESULTS

Under the Hartree-Fock (HF) theory, the many-body wave function takes the form

$$\Psi_{\text{HF}} = \frac{1}{\sqrt{N!}} \sum_P (-1)^P \phi_1(\vec{r}_1)\phi_2(\vec{r}_2)\ldots\phi_N(\vec{r}_N),$$

where P represents permutations, and ϕ_α's are single-particle orbitals that satisfy the following HF equations:

$$\left[-\frac{1}{2}\nabla^2 + i\tilde{\lambda}(-\partial_y\sigma_x + \partial_x\sigma_y) + \frac{1}{2}r^2 + \frac{g}{4}n(r) \right.$$
$$\left. - \frac{g}{4}\vec{m}(r) \cdot \vec{\sigma} \right]\phi_\alpha(\vec{r}) = \xi_\alpha\,\phi_\alpha(\vec{r}), \tag{4}$$

where

$$n(r) = \sum_{\alpha=1}^N |\phi_\alpha(\vec{r})|^2, \quad \vec{m}(r) = \sum_{\alpha=1}^N \phi_\alpha^\dagger(r)\vec{\sigma}\,\phi_\alpha(\vec{r})$$

are local density and spin vector, respectively.

We numerically solve the HF equations self-consistently *without* invoking the LLL approximation (for details, see
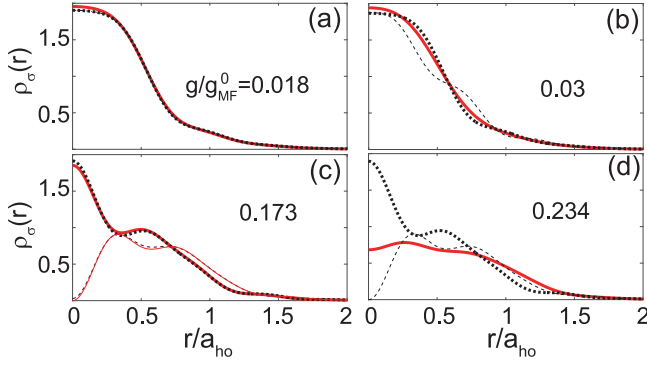
FIG. 4. Density profiles of each spin species for different interaction strengths with $N = 6$ and $\tilde{\lambda} = 7$, by both ED (red solid lines: thick lines for spin up and thin lines for spin down) and HF (black dashed lines: thick lines for spin up and thin lines for spin down) methods.

Appendix C). In Fig. 4 we plot density profiles from this calculation. Here we also take $N = 6$ and $\tilde{\lambda} = 7$ in order to make comparisons with the ED results. However, we also performed HF calculations up to $N = 200$ and found no qualitative differences from the $N = 6$ results presented here. For small interaction strength $g = 0.018 g_{MF}^0$ [Fig. 4(a)], both HF and ED tell us that the state is nonmagnetic with identical density profiles for both spin species. Furthermore, the results from the two theories agree with each other very well. At $g = 0.03 g_{MF}^0$ [Fig. 4(b)], ED predicts a nonmagnetic state, whereas HF indicates that the system already enters the ferromagnetic regime. In fact, HF calculation predicts a critical interaction strength $g_{HF} \approx 0.025 g_{MF}^0$, while the corresponding critical interaction strength for ED is $g_{ED} \approx 0.055 g_{MF}^0$. That $g_{ED} > g_{MF}$ can be attributed to the fact that the quantum correlation in the ED calculation disfavors the ferromagnetic phase. At $g = 0.173 g_{MF}^0$ [Fig. 4(c)], HF and ED agree with each again, both predicting a ferromagnetic state. At a large interaction strength $g = 0.234$ [Fig. 4(d)], discrepancies arise between the two calculations again: ED predicts a nonmagnetic state, while HF gives a ferromagnetic state. In fact, as we have expected, for $g > g_{HF}$, HF always predicts a ferromagnetic state. In contrast, our ED calculation shows that for large g, strong correlation destroys the ferromagnetic state.

In the phase diagram of Fig. 1, the dashed line represents g_{HF}, which separates the phase space into nonmagnetic (below the dashed line) and ferromagnetic regimes (above the dashed line). g_{HF} decreases quickly as $\tilde{\lambda}$ increases (which can again be understood as due to the band flattening), but never terminates as in the case of ED. To demonstrate further the effects of quantum correlation, we plot in Fig. 5 the energy as a function of interaction strength at $\tilde{\lambda} = 7$. Figure 5(a) shows how the total energy E_G, the kinetic energy E_{kin}, and the interaction energy E_{int} from the ED calculation change as g. As g increases, E_G keeps increasing monotonically, while E_{int} decreases at phase transition point (shown by the vertical lines) at a cost of increasing E_{kin}. In Fig. 5(b) we plot the ratio of the interaction energy, which is simply g times the density-density correlation between the two spin species integrated over all space, from the ED and the HF calculation. As it shows, in the weakly correlated nonmagnetic and ferromagnetic regimes, the ED
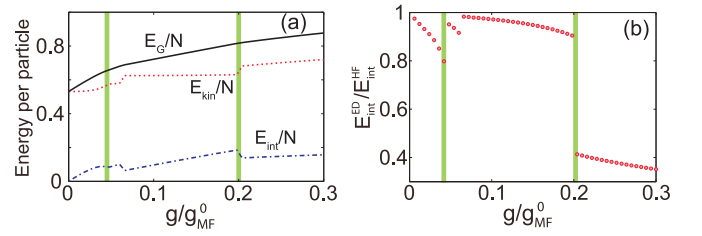

FIG. 5. (a) ED results for the ground-state energy E_G, the kinetic energy E_{kin}, and the interaction energy E_{int} as functions of interaction strength. (b) The ratio of the interaction energy from the ED calculation and that from the HF calculation. The two vertical lines separate the parameter space into three phases according to the ED calculation: from left to right, we have the weakly correlated nonmagnetic phase, the ferromagnetic phase, and the strongly correlated nonmagnetic phase. Here $N = 6$ and $\tilde{\lambda} = 7$.

and the HF results are comparable to each other. By contrast, in the strongly correlated regime, the interaction energy from the ED calculation is significantly lower than that from the HF calculation. This clearly shows how the system can develop nontrivial quantum correlations such that, even though the density profiles of the two spin species completely overlap with each other, the joint probability of finding two unlike spins at the same position is strongly suppressed. This indicates that microscopically the strongly correlated state is somewhat like the projected state proposed by Gutzwiller [18,19].

V. SCALING WITH PARTICLE NUMBER AND MULTIBAND EFFECTS

The previous sections have shown the interplay between Hartree-Fock interaction and strong correlation effects which is well controlled by the SO coupling strength. Their competition leads to the weakly and strongly correlated nonmagnetic state and chiral ferromagnetic state. Now we extend our previous findings to a larger particle number N regime. We first address this problem through the HF calculation and then ED calculation for smaller system size.

We present in Fig. 6(a) the critical interaction strength g_c characterizing the boundary between the weakly correlated nonmagnetic phase and the ferromagnetic phase, obtained by the HF calculation. For $N < N_{\tilde{\lambda}}$ where $N_{\tilde{\lambda}} \approx 2\sqrt{2}\tilde{\lambda}$ is roughly
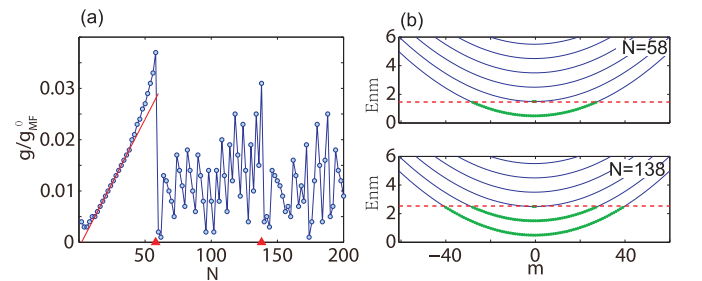

FIG. 6. (a) Critical interaction strength g_c for $\tilde{\lambda} = 20$, above which the system is ferromagnetic. The two red triangles indicate the position where a new Landau level starts to be populated. (b) The single-particle energy bands (solid curved lines) and the Fermi level (dashed horizontal lines) for $N = 58$ (upper panel) and $N = 138$ (lower panel).

the number of atoms that the LLL can host before the next Landau level is populated, the physics is dominated by the lowest Landau level as indicated by the upper panel in Fig. 6(b). We find that the critical interaction strength g_c is nearly linear with atom number N. This result is consistent with the Stoner's picture: g_c is proportional to the inverse of density of states near the Fermi level, where the density of states of the Landau level is roughly proportional $1/N$.

As the atom number increases further, the higher-lying Landau levels begin to be occupied. Meanwhile, new Fermi surfaces emerged. The multiband structure cut off the linear scaling relationship $g_c \propto N$. As shown in Fig. 6(a), the critical interaction strength has a steep drop whenever a new Landau level starts to be populated. This phenomenon may be attributed to the multiband structure. As a new Landau level is being occupied, a new Fermi surface with roughly the same density of states as the lowest one appears. Based on the intuitive Stoner's argument, the newly emerged Fermi surface drives the ferromagnetic transition at a smaller g_c. Hence whenever a newly occupied Landau level emerges, g_c exhibits a sudden drop. In between two such steep drops, g_c has a rather complicated dependence on N, probably due to the presence of multiple Fermi surfaces.

To check this idea by a full quantum treatment, we performed an ED calculation generalized to a two band model by including two lowest Landau levels. Results for the critical interaction strength g_c as a function of N is shown in Fig. 7(a). As long as only the LLL is populated ($N \leqslant 10$), we have roughly $g_c \propto N$, and g_c has a sudden drop as the second Landau level begins to be occupied. This is in full agreement with the HF result. In Fig. 7(b), we show the occupation on the two Landau levels for different fermion numbers with fixed $g = 0.2g_{\mathrm{MF}}^0$. It shows that as N increases from 6, the weight in the second band becomes larger but the system still stays at a nonmagnetic phase for $N \leqslant 10$. As N further increases, we find there are more occupations in the second band and the system becomes magnetic. This calculation ensures that for large particle numbers, the ferromagnetic phase can still be reached for a small interaction strength. In other words, the transition from the weakly correlated nonmagnetic phase to the ferromagnetic phase is *not* limited to small atom numbers.

Finally, we checked the importance of the quantum correlation with respect to the atom number N. We performed ED calculations for $N = 4, 6, 8$. The phase diagrams obtained for different particle numbers are shown in Fig. 8(a). We find that
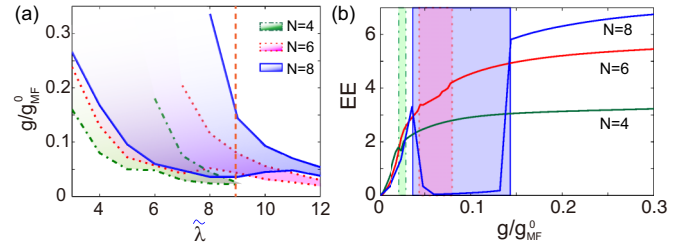
FIG. 8. (a) Ferromagnetic regime (shaded regions bounded between two lines) obtained by ED calculation for different atom number $N = 4$ (dash dotted lines), 6 (dotted lines), and 8 (solid lines). (b) The EE as a function of interaction strength for atom number $N = 4, 6, 8$ and SO coupling strength $\tilde{\lambda} = 9$ (indicated by the red dashed line in (a)). The shaded regime between two vertical lines indicate the ferromagnetic regimes for different N with the same corresponding line styles as in (a).

with increasing N, the quantum correlation effect is somewhat weakened and the regime where the mean-field theory applies is enlarged. Correspondingly, the ferromagnetic regime in the g-$\tilde{\lambda}$ phase diagram is enlarged with increasing N. In Fig. 8(b), we plot the entanglement entropy as a function of interaction strength for $\tilde{\lambda} = 9$ and atom number $N = 4, 6, 8$. We clearly find that as N increases, the EE is dramatically decreased in the ferromagnetic regime where the Hartree-Fock interaction dominates. Note that the mean-field HF calculation cannot capture the transition from the ferromagnetic to the strongly correlated nonmagnetic phase at an upper critical interaction strength. Hence how the upper critical interaction strength scales as N is beyond the scope of this work.

VI. EXPERIMENTAL DETECTION OF CHIRAL CURRENT

Finally, we propose an experimental procedure to detect the chiral current associated with the ferromagnetic state. The procedure goes as follows: First the ground state (either magnetic or not) is prepared. Then the harmonic trap is suddenly distorted from isotropic to anisotropic. For a nonmagnetic state, as shown in the upper panel of Fig. 9 obtained

FIG. 9. Time evolution of the atomic cloud after a sudden trap deformation. At $t = 0$, the trapping frequency along the y axis is suddenly changed from ω to 3.16ω, while that along the x axis remains at ω. The upper (lower) panel shows the dynamics of a nonmagnetic (ferromagnetic) state. Here $N = 6$, $\tilde{\lambda} = 7$, and $\tau_0 = 1/\omega$.
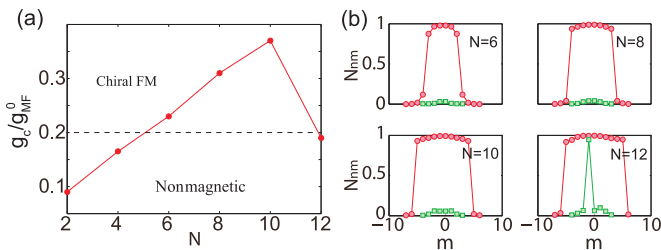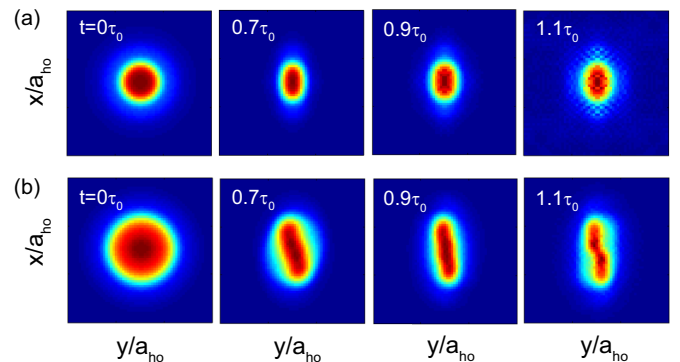

FIG. 7. (a) Critical interaction strength g_c obtained by ED calculation as a function of fermion number N with SO coupling strength fixed at $\tilde{\lambda} = 3$. (b) The occupation number in each band (red circles: lowest Landau level; green squares: second Landau level) shown for different particle numbers with $g = 0.2g_{\mathrm{MF}}^0$.
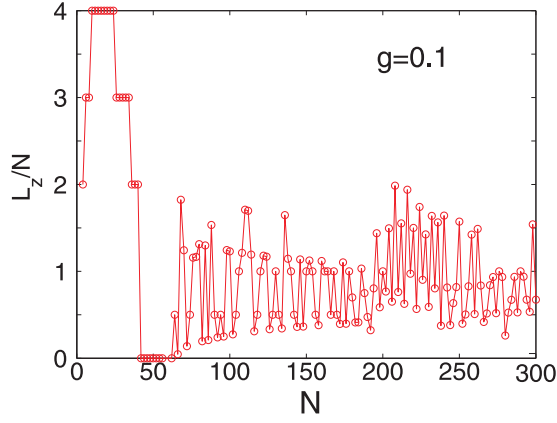
FIG. 10. Average angular momentum per particle L_z/N as a function of N. Note that the spin population oscillates in space such that the average spin per particle S_z/N is very small. Hence $L_z/N \approx J_z/N$. Here we fix the interaction strength $g = 0.1g_{MF}^0$, the trap frequency is scaled as $\omega = \omega_0/\sqrt{N}$, and the dimensionless SO coupling strength is scaled accordingly as $\tilde{\lambda} = \tilde{\lambda}_0 N^{1/4}$. In the calculation, we take $\tilde{\lambda}_0 = 6$.

from a time-dependent HF calculation (see Appendix D), this induces a quadrupole mode. By contrast, for an initial chiral ferromagnetic state, the whole cloud also undergoes an angular rotation, analogous to the scissors mode in a condensate with vortices [26].

We have carried out similar time-dependent HF calculations for particle numbers N up to a few hundred and find a very similar behavior as presented in Fig. 9. In Fig. 10, we present how the average angular momentum per particle L_z/N of the system scales with N. In this calculation, we fix the interaction strength $g = 0.1g_{MF}^0$, but scale the trap frequency as $\omega = \omega_0/\sqrt{N}$, where ω_0 is the trap frequency at $N = 1$. This scaling is to keep the density at the trap center as roughly a constant. As a consequence, the dimensionless SO coupling strength scales accordingly as $\tilde{\lambda} = M\lambda a_{ho}/\hbar^2 = \tilde{\lambda}_0 N^{1/4}$. Figure 10 shows that for large N such that multiple Landau levels are occupied, L_z/N oscillates, but exhibits no obvious decay for N up to 300. The oscillation in L_z/N can also be attributed to the multi-Landau-level effects. This gives further evidence that the chiral ferromagnetic state can survive for large particle numbers. Computational resource limits our calculation to $N = 300$. But this is not an unrealistic number. Note that, experimentally, a two-dimensional Fermi gas is obtained by tightly confining the atoms along the perpendicular direction. The atom number is restricted to $N \lesssim 10^3$ so that only the single-particle ground state in the tight confinement direction is occupied [27]. From a theoretical point of view, the physics discussed in our work relies on the Landau-level-like structure in the single-particle spectrum, which only exists in the presence of the harmonic trap. Hence it is not meaningful to take the $N \to \infty$ thermodynamic limit, under which the trap frequency vanishes.

VII. CONCLUSION

In summary, we have shown that how the Landau-level-like band structure of a 2D Rashba SO coupled Fermi gas, with a controllable band flatness, can be exploited to exhibit itinerant ferromagnetism. The near-flat band structure dramatically reduces the critical interaction strength required for the ferromagnetic phase transition. We employed two complementary methods, the fully quantum ED method and the mean-field HF method, to investigate this problem. Our calculation elucidates the interplay between the mean-field repulsion and the quantum correlation effects, and shows that the former favors while the latter tends to destroy ferromagnetism. The emergence and disappearance of the ferromagnetic phase result from the competition between these two factors. We have also shown that the ferromagnetic phase in our system is accompanied by a chiral density current resulting from the SO coupling, and proposed a way to detect this current in experiment. We hope our work may open avenues of research in both SO coupling and itinerant magnetism in cold atoms.

Finally, we comment that Dresselhaus SO coupling has recently been realized by the Shanxi group [28,29]. The single-particle spectrum of a harmonically trapped 2D spin-1/2 particle remains exactly the same if the Rashba SO coupling is changed to the Dresselhaus coupling. Our results for the repulsive Fermi gas remain essentially the same under Dresselhaus coupling (see Appendix E). The only difference would be the spin texture of the ferromagnetic state as shown in Fig. 3(b).

APPENDIX A: EXACT DIAGONALIZATION SCHEME

For a single spin-1/2 particle with Rashba spin-orbit (SO) coupling confined in a two-dimensional (2D) isotropic harmonic trap, the single-particle Hamiltonian is given by $\mathcal{H}_0$ in the main text. The spatial wave function of the eigenstates take the form

$$\Phi_{n,m}(\vec{r}) = \begin{pmatrix} f_{nm}(r) \\ g_{nm}(r)e^{i\phi} \end{pmatrix} e^{im\phi},$$

$$\Phi_{n,-m-1}(\vec{r}) = \begin{pmatrix} g_{nm}(r)e^{-i\phi} \\ -f_{nm}(r) \end{pmatrix} e^{-im\phi}, \quad \text{(A1)}$$

$$n = 0,1,2,\ldots; \ m = 0, \pm 1, \pm 2, \ldots,$$

which form a degenerate time-reversed pair with eigenenergies $\epsilon_{n,m} = \epsilon_{n,-m-1}$. In the limit that the dimensionless SO coupling strength $\tilde{\lambda} \gg 1$, the eigenenergies (apart from a constant) take the following approximate form:

$$\epsilon_{n,m} = \epsilon_{n,-m-1} \approx \left[n + \frac{m(m+1)}{2\tilde{\lambda}^2} \right] \hbar\omega.$$

For a few-body system with weak interaction and small particle number, the Hilbert space is limited to the lowest Landau level (LLL) which is specified by the quantum number $n = 0$. We introduce a cutoff m^* which further reduces the Hilbert space to that with $-m^* - 1 < m < m^*$. The value of m^* is determined

by values of N and g. Specifically, we first make sure that the single-particle energy for the m^* state is well below the next Landau level. After the calculation is done and the ground state $|G\rangle$ is found, we calculate the occupation number for single-particle states m which is given by $n_m = \langle G|c_m^\dagger c_m|G\rangle$ and make sure that n_m is small near the cutoff values of m^* and $-m^* - 1$. Finally, we also vary m^* to make sure that our results do not depend on the choice of the cutoff. Given N fermionic particles filled to $M = 2m^* + 2$ single-particle states, we obtain totally $\frac{M!}{N!(M-N)!}$ Fock states. Due to the rotational symmetry of this system, we are able to divide the full truncated Hilbert space into several independent subspaces with fixed total angular momentum $J_z = \sum_{i=1}^{N}(m_i + \frac{1}{2})$, which considerably reduces the dimension of the Hamiltonian that needs to be diagonalized.

Next we present the main steps for the ED scheme for specific subspace with J_z and particle number N. The Fock states are denoted by $|p_i\rangle = a_{m_1}^\dagger a_{m_2}^\dagger \ldots a_{m_N}^\dagger |0\rangle, i = 1, 2, \ldots, D$ with the convention $m_1 < m_2 < \cdots < m_N$. For later use, we associate each occupied single-particle state m_i with a number N_{m_i} (for example, $N_{m_1} = 1$). The single-particle part of the Hamiltonian $\mathcal{H}_0$ is diagonal under this basis:

$$\langle p_i|\mathcal{H}_0|p_j\rangle = \sum_{\alpha=1}^{N} \epsilon_{m_\alpha}\delta_{ij}, \tag{A2}$$

where $\epsilon_m = \epsilon_{n=0,m}$. Under the same basis, the diagonal matrix elements of the interacting Hamiltonian $\mathcal{H}_{\rm int}$ take the form

$$\langle p_i|\mathcal{H}_{\rm int}|p_i\rangle = \frac{g}{4}\int d^2\vec{r}\,(\rho^2 - \vec{s}^2), \tag{A3}$$

where $\rho(r) = \langle p_i|\hat{\rho}|p_i\rangle$ and $\vec{s} = \langle p_i|\hat{\vec{s}}|p_i\rangle$ represent the local density and spin vector, respectively. This diagonal matrix element can be regarded as the mean-field Hartree-Fock interaction energy associated with the Fock state $|p_i\rangle$. The nondiagonal matrix elements of $\mathcal{H}_{\rm int}$ are nonvanishing only between two Fock states that differ by two single-particle states, say $|p\rangle = \ldots a_m^\dagger \ldots a_n^\dagger \ldots |0\rangle$ and $|q\rangle = \ldots a_k^\dagger \ldots a_l^\dagger \ldots |0\rangle$ with the constraint $m + n = k + l$:

$$\langle q|\mathcal{H}_{\rm int}|p\rangle = (-1)^{N_m+N_n+N_k+N_l}g\int d^2\vec{r}\,[\Psi_{l\uparrow}^*\Psi_{k\downarrow}\Psi_{m\downarrow}\Psi_{n\uparrow} \\ + \Psi_{k\uparrow}^*\Psi_{l\downarrow}\Psi_{n\downarrow}\Psi_{m\uparrow} - \Psi_{k\uparrow}^*\Psi_{l\downarrow}\Psi_{m\downarrow}\Psi_{n\uparrow} \\ - \Psi_{l\uparrow}^*\Psi_{k\downarrow}\Psi_{n\downarrow}\Psi_{m\uparrow}],$$

where $\Psi_{m\sigma}, \sigma = \uparrow, \downarrow$ denotes the wave function of the single-particle state in the lowest Landau level. The nondiagonal part of $\mathcal{H}_{\rm int}$ builds up correlations between different Fock states. It mixes Fock states with different spin polarization and therefore tends to suppress the magnetic phase.

APPENDIX B: CALCULATION OF ENTANGLEMENT ENTROPY (EE)

The entanglement measure is useful to analyze correlation properties of the ground state. We calculate EE in the following way. We first divide the system into two subsystems (denoted as A and B) and then analyze the reduced density matrix in one of the subsystems. In our system, the subsystems can be distinguished by the single-particle angular momentum

$j_z = m + \frac{1}{2}$: subsystem A includes all the positive j_z states, while subsystem B includes all the negative j_z states. The total ground-state density matrix is given by $\rho = |G\rangle\langle G|$ with $|G\rangle$ denoting the ground state. By the standard procedure, we trace out subsystem B to find the reduced density matrix for subsystem A:

$$\rho^A = \sum_{n_{-j_c},\ldots,n_{-1/2}} \langle n_{-j_c},n_{-j_c+1},\ldots,n_{-1/2}| \\ \times |\rho|n_{-j_c},n_{-j_c+1},\ldots,n_{-1/2}\rangle, \tag{B1}$$

where $j_c = m_c + 1/2$ denotes a finite-size cutoff of this system. The eigenvalues of the reduced density matrix ρ_i^A give rise to the entanglement spectrum $\xi_i = -\ln\rho_i^A$. For a pure Fock state without any correlation, there will be only one nonzero eigenvalue $\rho_i^A = 1$ and all the others are equal to zero. Therefore, we can observe only one point with $\xi_i \sim 0$ and other points $\xi_i \gg 1$ in the entanglement spectrum for a less correlated ground state, while for a strongly correlated ground state, the entanglement spectrum has a broad and flat structure. We can further calculate the ground state EE by $\mathrm{EE} = -\mathrm{tr}\rho^A\ln\rho^A = -\sum_i \rho_i^A\ln\rho_i^A$. We will find $\mathrm{EE} \sim 0$ for a less correlated ground state while $\mathrm{EE} \gg 1$ for a strongly correlated ground state.

APPENDIX C: HARTREE-FOCK EQUATION FOR TRAPPED SPIN-ORBIT COUPLED FERMI GAS

For weakly correlated states, the mean-field Hartree-Fock (HF) approximation captures the key physics. The HF approximation neglects quantum correlations of the state by assuming

$$\Psi_{\rm HF} = \frac{1}{\sqrt{N!}}\sum_P (-1)^P \phi_1(\vec{r}_1)\phi_2(\vec{r}_2)\ldots\phi_N(\vec{r}_N), \tag{C1}$$

where P denotes all permutations, and ϕ_α's are orthonormal single-particle orbitals to be determined. With this assumption, we can obtain the HF Hamiltonian as follows (adopting the trap units):

$$H_{\rm HF} = \int d^2\vec{r}\,\psi^\dagger\left[-\frac{1}{2}\nabla^2 + i\tilde{\lambda}(-\partial_y\sigma_x + \partial_x\sigma_y) + \frac{1}{2}r^2 \\ + \frac{g}{4}n(r) - \frac{g}{4}\vec{m}(r)\cdot\vec{\sigma}\right]\psi, \tag{C2}$$

where the constant terms $(g/4)\int dr[\vec{m}(r)^2 - n(r)^2]$ have been dropped, and $n(r)$, $\vec{m}(r)$ are respectively the averaged local density and spin vector:

$$n(r) = \sum_{\alpha=1}^{N}|\phi_\alpha(\vec{r})|^2, \quad \vec{m}(r) = \sum_{\alpha=1}^{N}\phi_\alpha^\dagger(\vec{r})\,\vec{\sigma}\,\phi_\alpha(\vec{r}). \tag{C3}$$

To manipulate the interaction term in a spin rotational invariant way, we have rewritten the interaction term as $\frac{g}{8}\int dr(n^2 - \vec{s}^2)$ in the above calculation. The single-particle wave functions ϕ_α with $\alpha = 1, 2, \ldots, N$ satisfy the HF equations:

$$\left[-\frac{1}{2}\nabla^2 + i\tilde{\lambda}(-\partial_y\sigma_x + \partial_x\sigma_y) + \frac{1}{2}r^2 + \frac{g}{4}n(r) \\ - \frac{g}{4}\vec{m}(r)\cdot\vec{\sigma}\right]\phi_\alpha(\vec{r}) = \xi_\alpha\,\phi_\alpha(\vec{r}), \tag{C4}$$

which, together with Eq. (C3), form a closed set and can be solved self-consistently.

In our calculation, ϕ_α's are expanded onto the single-particle eigenstates defined in Eq. (A1): $\phi_\alpha(r) = \sum_{nm} u_{\alpha;nm} \Phi_{n,m}(r)$. Note that in our HF calculation, we do not restrict to the LLL. So we have to introduce a cutoff N_c for quantum number n, in addition to the cutoff for quantum number m. Under this expansion, the HF equations take the form

$$\sum_{n_2=1}^{N_c} \left(\epsilon_{n_1 m} \delta_{n_1 n_2} + \frac{g}{4} N^m_{n_1 n_2} - \frac{g}{4} S^m_{n_1 n_2} \right) u_{\alpha;n_2 m} = \xi_\alpha u_{\alpha;n_1 m},$$

(C5)

where $N^m_{n_1 n_2} = \int d^2\vec{r} \, \Phi^\dagger_{n_1,m} \Phi_{n_2,m} n(r)$, $S^m_{n_1 n_2} = \int d^2\vec{r} \, \Phi^\dagger_{n_1,m} \vec{\sigma} \Phi_{n_2 m} \cdot \vec{m}(r)$. Due to the rotational symmetry, m is a conserved quantum number. The Hartree-Fock wave function $\Psi_{\rm HF}$ would be obtained through iteratively solving the above equations until self-consistency is reached. While the ED calculation can only handle a few particle numbers (up to eight in our calculation), we have done HF calculations up to 200 particle numbers. From our calculation, we found that the mean-field critical interaction strength at which the nonmagnetic state changes to a ferromagnetic state roughly scales as $g_{\rm HF} \propto N/\tilde{\lambda}^2$.

APPENDIX D: TIME-DEPENDENT HARTREE-FOCK THEORY

To study the dynamics, we extend the HF calculation to a time-dependent situation. The time-dependent Hartree-Fock equations take the form

$$\left(-\frac{1}{2}\nabla^2 + i\tilde{\lambda}(-\partial_y \sigma_x + \partial_x \sigma_y) + V(\vec{r},t) \right.$$
$$\left. + \frac{\kappa}{4}[n(r,t) - \vec{m}(r,t)\cdot\vec{\sigma}] \right) \phi_\alpha(\vec{r},t) = i\partial_t \phi_\alpha(\vec{r},t), \quad \text{(D1)}$$

where we have assumed that the trapping potential $V(\vec{r},t)$ is time dependent. The initial wave function at $t=0$ is taken as the ground-state wave function under $V(\vec{r},t=0)$. The orthonormality of the single-particle orbitals $\phi_\alpha(\vec{r},t)$ at time t is guaranteed by the unitary time evolution. The local
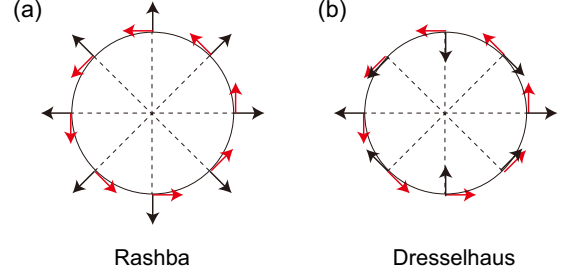

FIG. 11. The schematic plot of the spin polarization (black arrow) and density current (red arrow) for (a) Rashba SO coupled system and (b) Dresselhaus SO coupled system, respectively.

density and spin vector n and $\vec{m}$ are still given by Eqs. (C3) with the explicit time dependence.

APPENDIX E: MAPPING TO DRESSELHAUS SO COUPLING

In our calculation, we have taken the SO coupling to be of Rashba form: $\mathcal{V}_{\rm soc} = \lambda(p_y\sigma_x - p_x\sigma_y)$. The results can be easily generalized if the SO coupling is of Dresselhaus form: $\mathcal{V}^D_{\rm SO} = \lambda(p_y\sigma_x + p_x\sigma_y)$. The system with Dresselhaus SO coupling can be mapped to a system with Rashba SO coupling through a unitary transformation in spin space: $U = i\sigma_x$, under which the Pauli matrices are transformed as

$$\sigma_x \to \sigma_x, \quad \sigma_y \to -\sigma_y, \quad \sigma_z \to -\sigma_z,$$

and the Rashba SO coupling is then transformed to the Dresselhaus form. The s-wave interaction is spin SU(2) invariant and will not be changed under the above unitary transformation. So, all the results achieved in our main text hold for the Dresselhaus SO coupling case after this spin space transformation. For example, the single-particle wave function is obtained by $i\sigma_x \Phi_{n,m}(\vec{r})$, and the single-particle and many-body energy spectra are unchanged. The main difference is the change of the ground-state spin texture, where the local spin transforms as

$$s_x \to s_x, \quad s_y \to -s_y, \quad s_z \to -s_z,$$

as schematically shown in Fig. 11. The density current operator coming from the Dresselhaus SO coupling is also modified to be $\vec{j}^{(D)}_s = \lambda(s_y,s_x,0)$, which keeps the density current in the ground state invariant (Fig. 11).

[1] J. Dalibard, F. Gerbier, G. Juzeliūnas, and P. Öhberg, Rev. Mod. Phys. **83**, 1523 (2011).

[2] N. Goldman, G. Juzeliūnas, P. Öhberg, and I. B. Spielman, Rep. Prog. Phys. **77**, 126401 (2014).

[3] Y. J. Lin, K. Jiménez-García, and I. B. Spielman, Nature (London) **471**, 83 (2011).

[4] P. Wang, Z. Q. Yu, Z. Fu, J. Miao, L. Huang, S. Chai, H. Zhai, and J. Zhang, Phys. Rev. Lett. **109**, 095301 (2012).

[5] L. W. Cheuk, A. T. Sommer, Z. Hadzibabic, T. Yefsah, W. S. Bakr, and M. W. Zwierlein, Phys. Rev. Lett. **109**, 095302 (2012).

[6] M. Z. Hasan and C. L. Kane, Rev. Mod. Phys. **82**, 3045 (2010).

[7] X. L. Qi and S. C. Zhang, Rev. Mod. Phys. **83**, 1057 (2011).

[8] J. Zhang, H. Hu, X. J. Liu, and H. Pu, in *Annual Review of Cold Atoms and Molecules*, edited by K. Madson, K. Bongs, L. D. Carr, H. Zhai, and A. M. Rey (World Scientific, Singapore, 2014), Chap. 2.

[9] H. Zhai, Rep. Prog. Phys. **78**, 026001 (2015).

[10] M. J. Edmonds, M. Valiente, G. Juzeliūnas, L. Santos, and P. Öhberg, Phys. Rev. Lett. **110**, 085301 (2013).

[11] L. Dong, L. Zhou, B. Wu, B. Ramachandhran, and H. Pu, Phys. Rev. A **89**, 011602(R) (2014); L. Dong, C. Zhu, and H. Pu, Atoms **3**, 182 (2015).

[12] C. Wu, I. Mondragon-Shem, and X.-F. Zhou, Chin. Phys. Lett. **28**, 097102 (2011).

[13] H. Hu, B. Ramachandhran, H. Pu, and X.-J. Liu, Phys. Rev. Lett. **108**, 010402 (2012).

[14] B. Ramachandhran, H. Hu, and H. Pu, Phys. Rev. A **87**, 033627 (2013).

[15] E. Stoner, Philos. Mag. **15**, 1018 (1933).

[16] G.-B. Jo, Y.-R. Lee, J.-H. Choi, C. A. Christensen, T. H. Kim, J. H. Thywissen, D. E. Pritchard, and W. Ketterle, Science **325**, 1521 (2009).

[17] C. Sanner, E. J. Su, W. Huang, A. Keshet, J. Gillen, and W. Ketterle, Phys. Rev. Lett. **108**, 240404 (2012).

[18] M. C. Gutzwiller, Phys. Rev. Lett. **10**, 159 (1963); Phys. Rev. **137**, A1726 (1965).

[19] H. Zhai, Phys. Rev. A **80**, 051605(R) (2009).

[20] D. Bohm, Phys. Rev. **75**, 502 (1949).

[21] Y. Ohashi and T. Momoi, J. Phys. Soc. Jpn. **65**, 3254 (1996).

[22] For a mesoscopic finite-sized system, a generalized Bloch-Bohm theorem states that there exists an upper bound for the circulating current. See, for example, G. Vignale, Phys. Rev. B **51**, 2612 (1995).

[23] G. J. Conduit, Phys. Rev. A **82**, 043604 (2010).

[24] A. Ambrosetti, G. Lombardi, L. Salasnich, P. L. Silvestrelli, and F. Toigo, Phys. Rev. A **90**, 043614 (2014).

[25] S. Pilati, I. Zintchenko, and M. Troyer, Phys. Rev. Lett. **112**, 015301 (2014).

[26] C. Lobo, A. Sinatra, and Y. Castin, Phys. Rev. Lett. **92**, 020403 (2004); C. Lobo and Y. Castin, Phys. Rev. A **72**, 043606 (2005).

[27] P. Dyke, E. D. Kuhnle, S. Whitlock, H. Hu, M. Mark, S. Hoinka, M. Lingham, P. Hannaford, and C. J. Vale, Phys. Rev. Lett. **106**, 105304 (2011).

[28] L. Huang, Z. Meng, P. Wang, P. Peng, S.-L. Zhang, L. Chen, D. Li, Q. Zhou, and J. Zhang, Nat. Phys., doi:10.1038/nphys3672 (2016).

[29] Z. Meng, L. Huang, P. Peng, D. Li, L. Chen, Y. Xu, C. Zhang, P. Wang, and J. Zhang, arXiv:1511.08492.